



*Supplement of*

## **Landslides as geological hotspots of CO<sub>2</sub> emission: clues from the instrumented Séchilienne landslide, western European Alps**

**Pierre Nevers et al.**

*Correspondence to:* Pierre Nevers ([pierre.nevers@univ-fcomte.fr](mailto:pierre.nevers@univ-fcomte.fr))

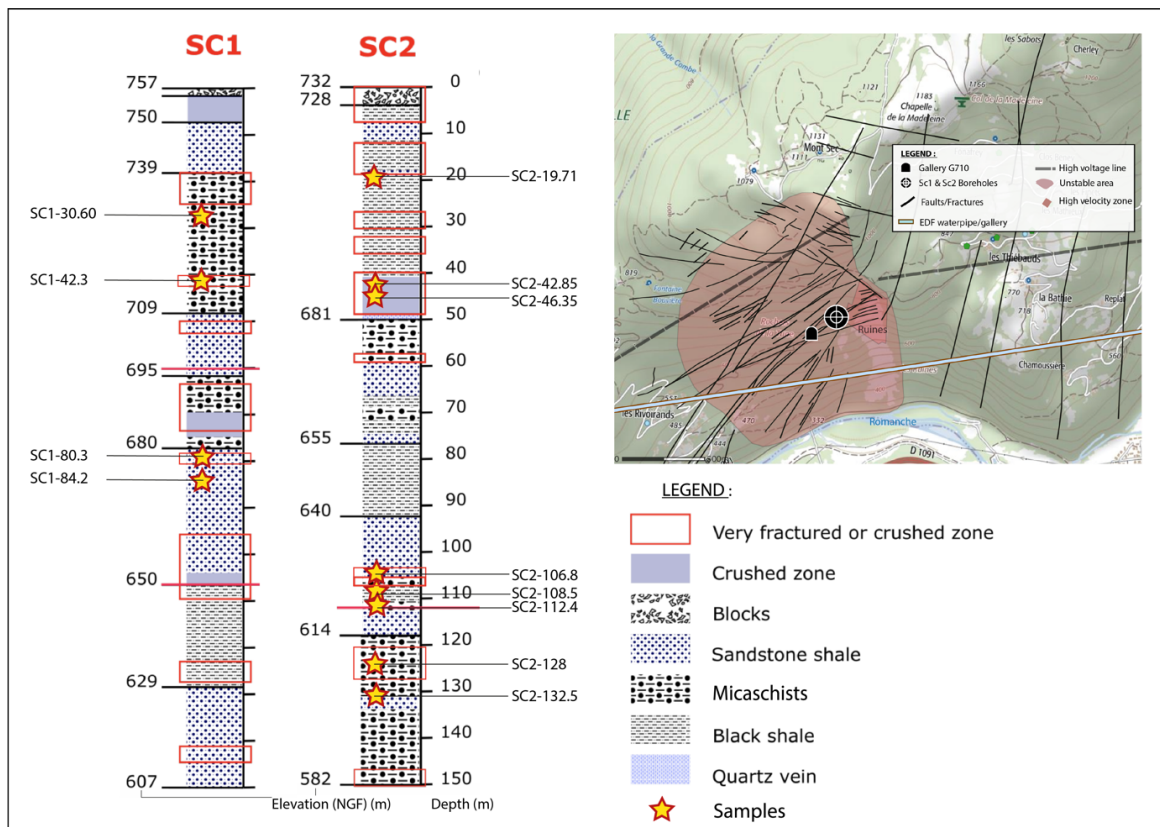
The copyright of individual parts of the supplement might differ from the article licence.

**Section S1. Petrological and mineralogical analysis of rock samples from the S chilienne slope: thin sections and X-ray diffraction (XRD)**

55

**Sampling:**

Samples used for this work were selected on the basis of their rock type, fracturation, and weathering degree in order to characterize the mineralogical, petrological, and geochemical modifications between fractured/weathered and unweathered samples of rocks from the same lithology. Thus, pairs and triplets of samples from the same lithology were collected, with various weathering degrees. The selected samples are represented as stars in the borehole logs (Fig. S1). Boreholes, as well as the lithological descriptions of the facies recovered by the core samples were carried out by the engineering consultant GEOTEC.



65

Figure S1: Boreholes SC1 and SC2 with location, lithology and analyzed samples location along the boreholes (Lithological profiles are modified from Lajaunie et al. (2019) and map is sourced from  IGN)

On the SC1 borehole (Fig. S1), 2 pairs of samples we selected, i.e. 4 samples to be studied:

- 70 - **(SC1 30.60 - 42.3):** recovered from micaschists, are blue-grey colored and show brown weathering and oxidation shades, crossed by several quartz veins. These micaschists present decimetric fractured levels, notably between 40.15 and 45.00 m depth. SC1-30.60 is the unweathered sample and SC1-42.3 is the weathered sample.
- 75 - **(SC1 84.2 - 80.3):** were sampled from massive, grey-blue micaschists with some pyrite and quartz, with punctual brown oxidation halos. From 79.20 to 81.40 m, a highly weathered and crushed zone is noticed within these micaschists. SC1-84.2 is the unweathered sample and SC1-80.3 is the weathered sample.

Two triplets and one pair of samples were selected from the second borehole (SC2), following the same logics as above. For the sample triplets, we selected one sample characterized as healthy and the other two were described as weathered:

- 80 - **(SC2 19.71 - 42.85 - 46.35)**: correspond to lustrous grey to black, vertically foliated and compact schists with quartz veins. The two altered samples are part of a very destructured and crushed zone with a brown to ochre clay matrix, made of weathered micaschist with sandstone occurrences, anthracite grey veins of quartz, hematite, goethite and disseminated pyrite. SC2-19.71 is the unweathered sample and SC2-42.85 and SC2-46.35 are the weathered samples.
- 85 - **(SC2 108.5 - 106.8)**: correspond to a zone made of an alternance of schists and light grey sandstones, with occasional anthracite black schists. Numerous centimetric to decimetric quartz veins are present as well as highly fractured oxidized zones with ochre clayey fillings, mostly from 105.90 to 107.50 m, from which the weathered samples are taken. SC2-108.5 is the unweathered sample and SC2-106.8 is the weathered sample.
- 90 - **(SC2 132.5 - 128 - 112.4)**: were sampled from light grey siliceous sandstones and shales, alternating with black shale levels. Numerous centimetric to decimetric quartz veins or interbeds and ochre oxidized fractures with red clayey fillings are noticed from 111.05 to 112.95 m. SC2-132.5 is the unweathered sample and SC2-128 and SC2-112.4 are the weathered samples.

Thin sections from these samples are shown in Fig. S2-S4. Overall, the unweathered and weathered samples present the same mineralogy, i.e. quartz, white micas, alkali feldspar more or less weathered into a clay phase, and “opaques” corresponding to sulfides and oxides. Observations of these “opaques” in reflected light allow us to identify the presence of highly-oxidized pyrite and chalcopyrite. This oxidation is characterized by iron oxides such as hematite. The difference between unweathered samples and weathered samples is the fractional contribution of these minerals. Indeed, in weathered samples, larger amounts of white mica and with lesser amounts of alkali feldspar are found, as well as more hematite.

100 Weathered samples present oxidized pyrite and chalcopyrite, which are not oxidized in the unweathered samples. Regarding the structures the sample, we do not observe any real difference between weathered and unweathered samples, except for the pair SC1 132.5 - 128 which seems to present a foliation for the fractured and weathered samples. This foliation is underlined by the white mica, forming flaps (figures S2 - S4).

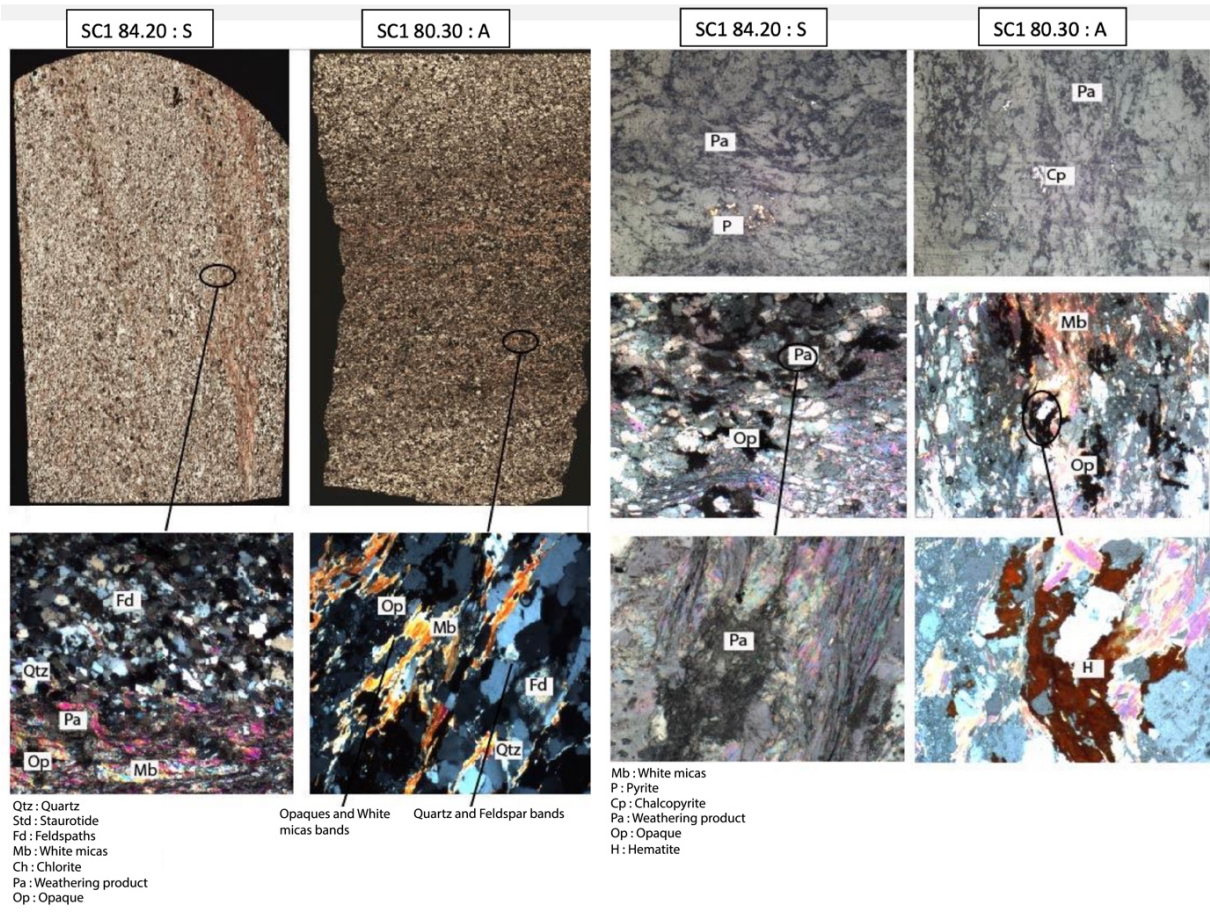


Figure S2: Thin sections photographs and mineralogy SC1 84.20-80.30

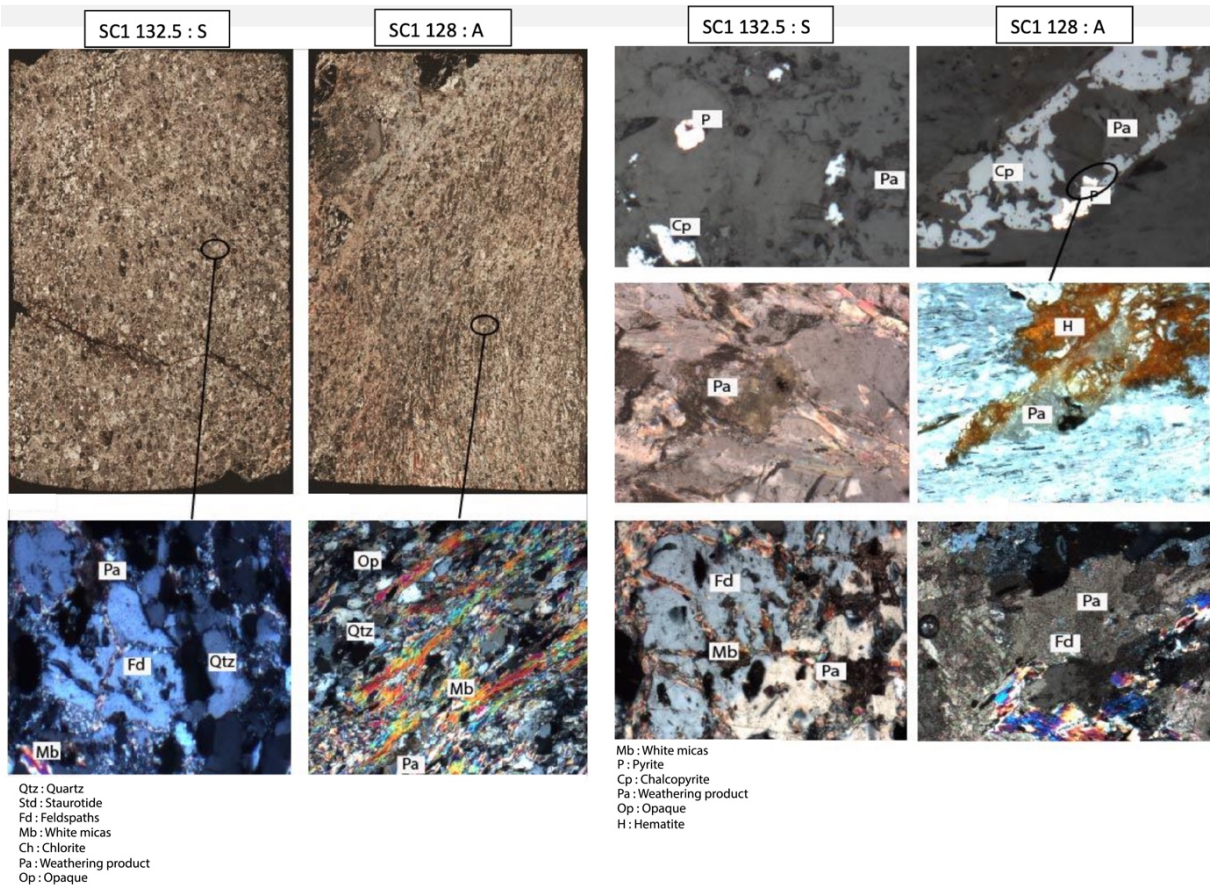
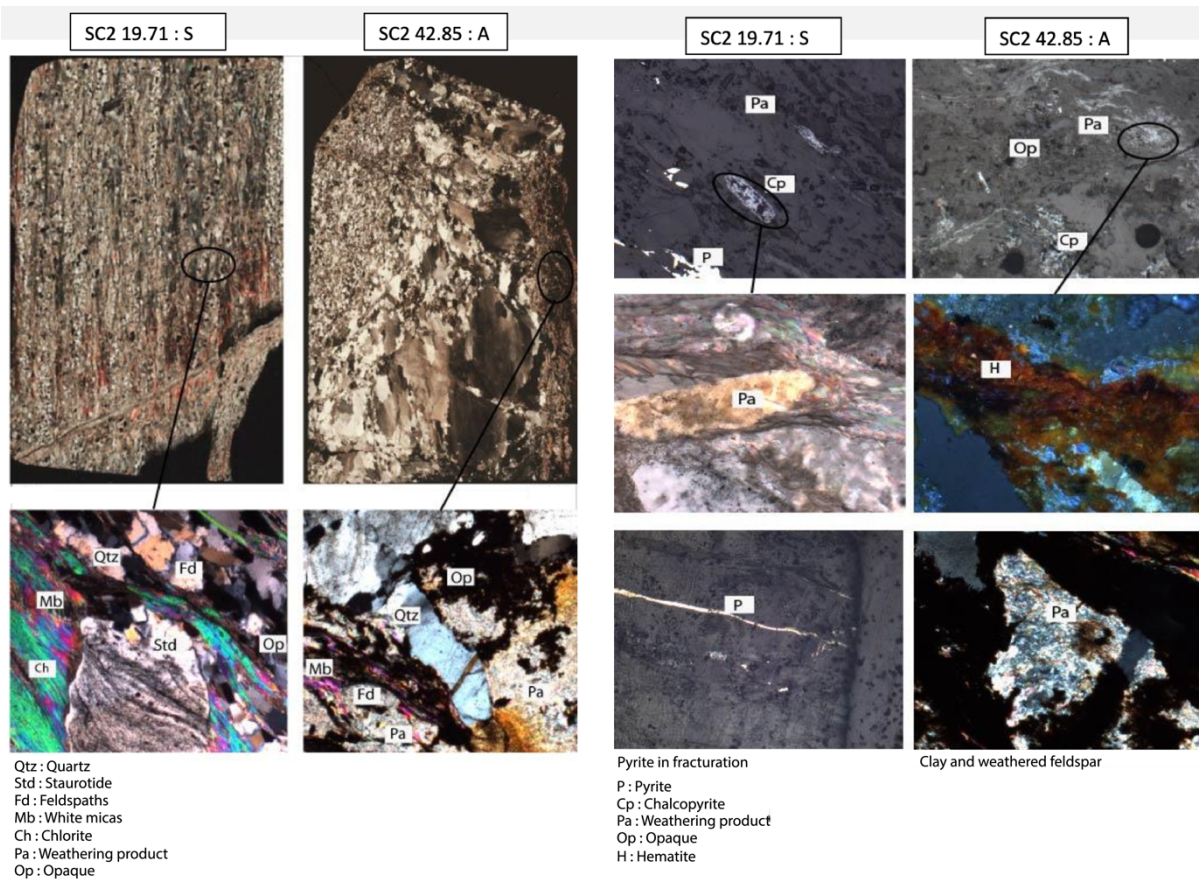


Figure S3: Thin sections photographs and mineralogy SC1 132.5-128



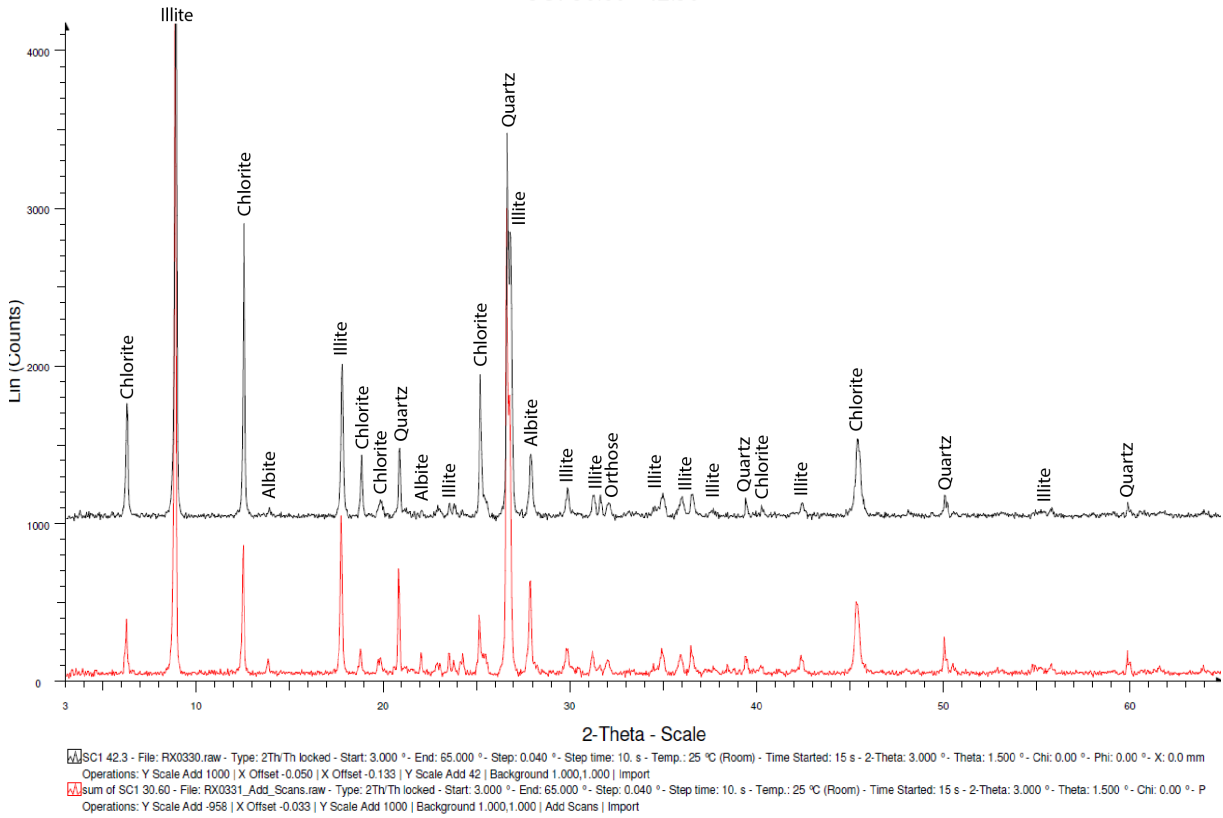
110

Figure S4: Thin sections photographs and mineralogy SC2 19.71-42.85

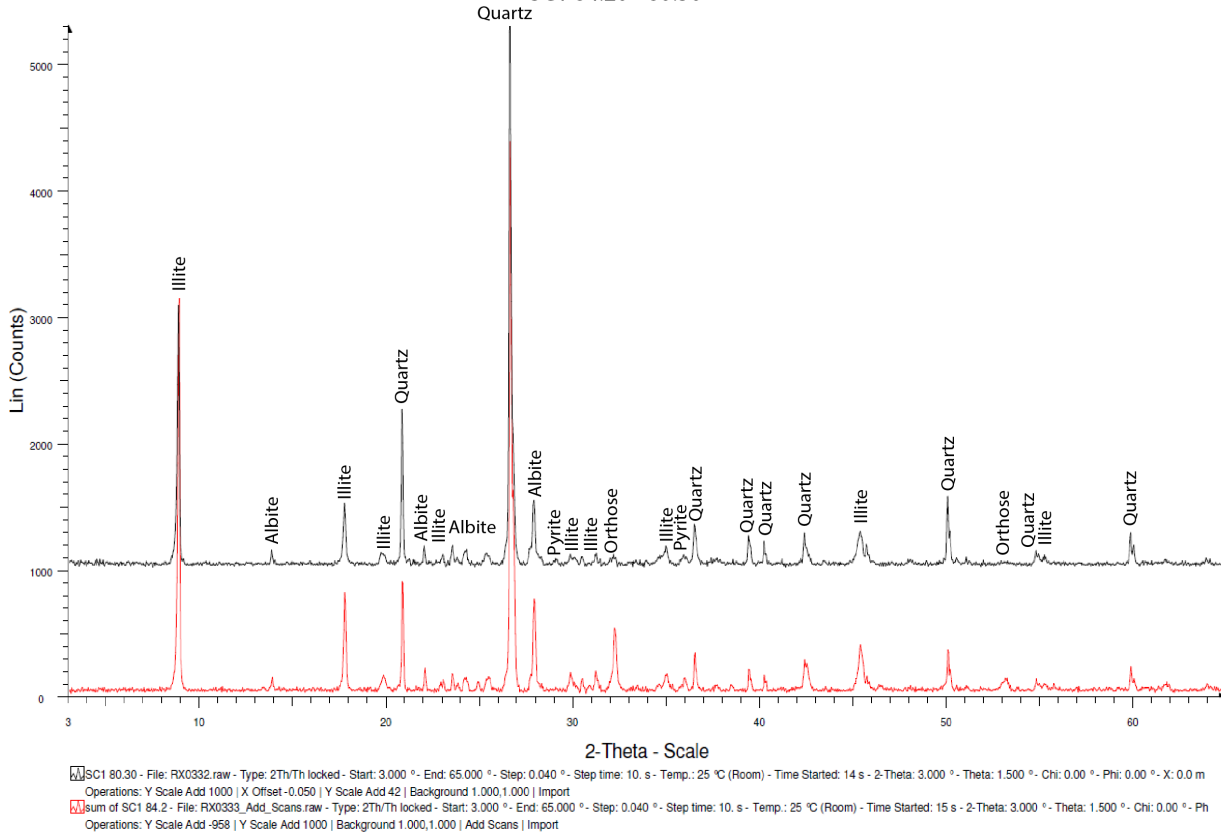
XRD analyses show that illite is the main type of white mica present in these samples, while albite and orthose are present as alkali feldspar (figures S5 - S7). Because of their low abundance in the samples, sulfides and oxides visible in thin sections are not to prominent in XRD. Overall, we observe lower amounts (up to complete disappearance) of orthose in the weathered samples compared to unweathered samples. In weathered samples, an increase of the proportion of illite and the appearance of hematite is evidenced (figures S5 - S7).

115

SC1 30.60 - 42.30



SC1 84.20 - 80.30



120 Figure S5: X-ray diffraction spectra SC1 30.60-42.30 / SC1 84.20-80.30

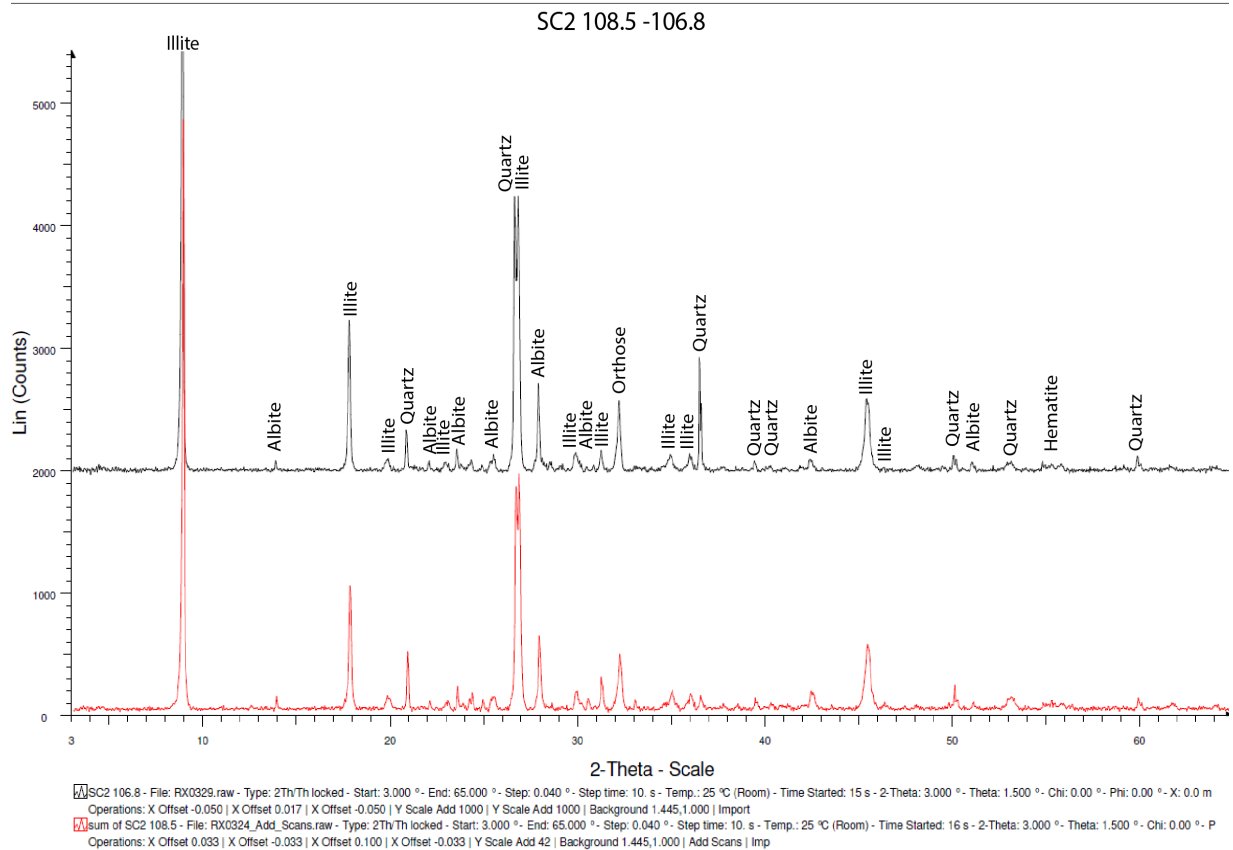
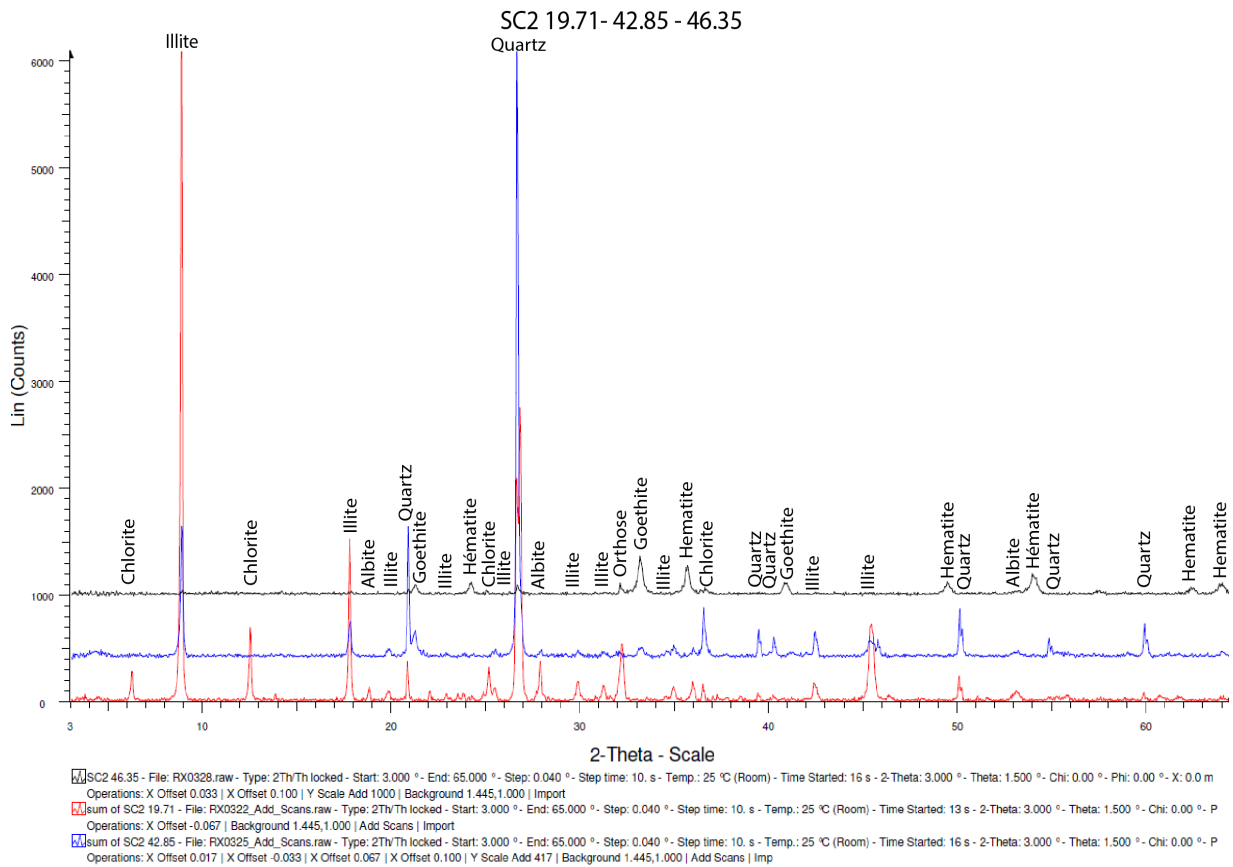
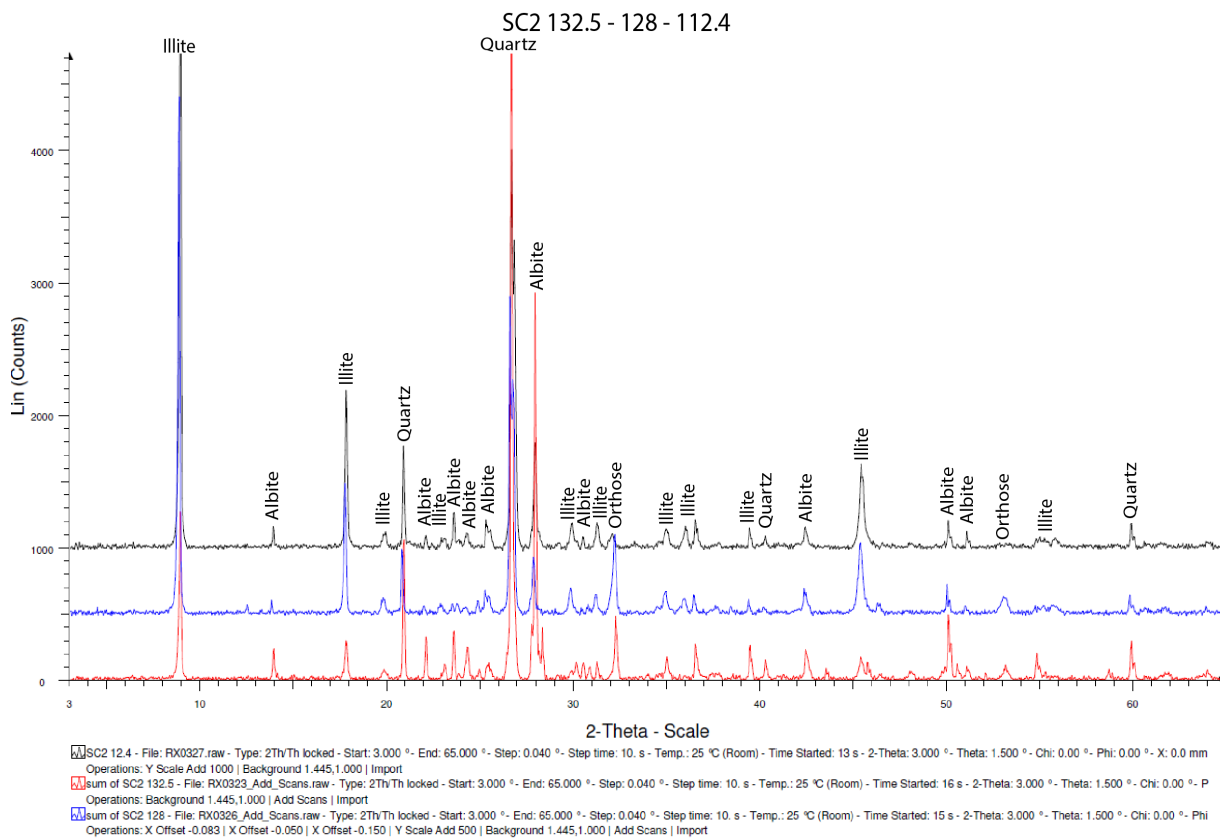


Figure S6: X-ray diffraction spectra SC2 19.71-42.85-46.35 / SC2 108.5-106.8



130

Figure S7: X-ray diffraction spectra SC2 132.5-128-112.4

135

140

145

150

155

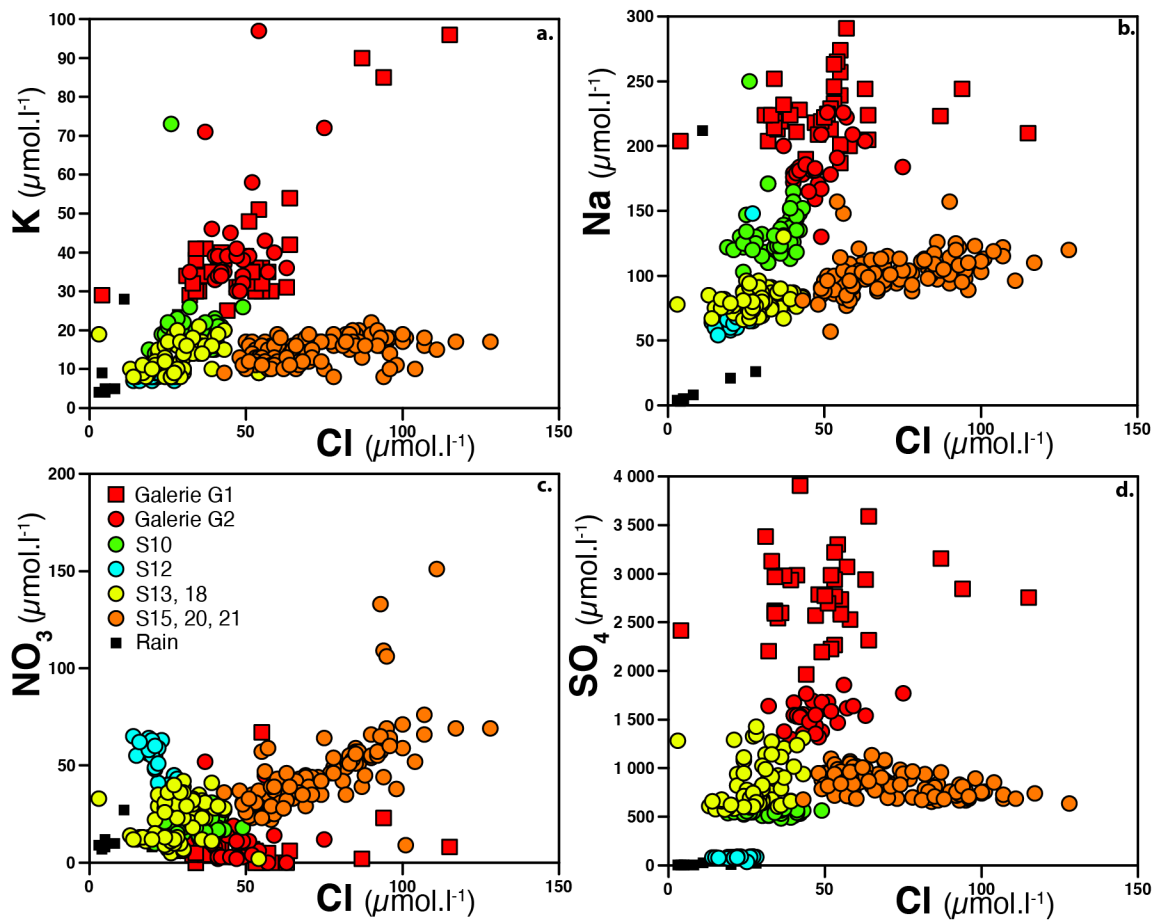


Figure S8: Elemental concentrations (X) of the different groups of water outflow from the S echilienne massif as a function of Cl concentrations; a. K vs. Cl, b. Na vs. Cl, c.  $\text{NO}_3$  vs. Cl, d.  $\text{SO}_4$  vs. Cl. These diagrams are used in the section 5.1.1. of the main text.

160

165

170

### Section S3. Solving the mixing equations

175 *Model set-up and Sr fractions*

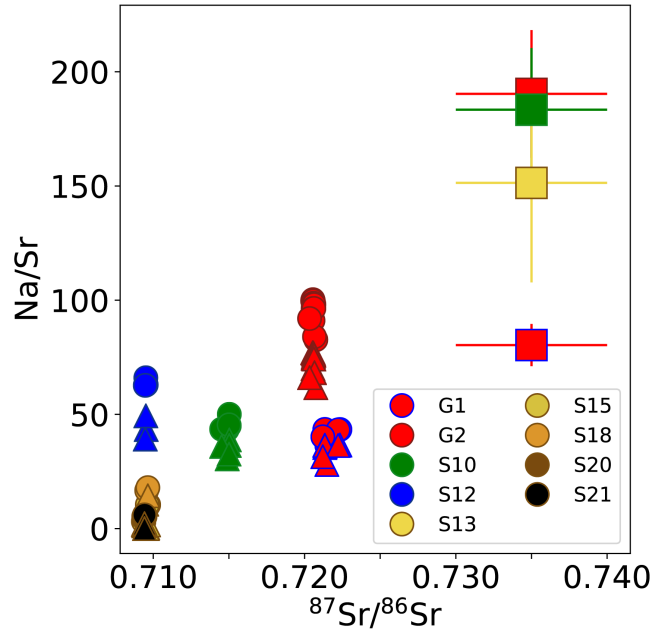
Given the discussion of section 5.1 and the geochemical mixing diagrams presented in Fig. 4, three end members can be identified to release solutes to the springs of the S echilienne area: silicate weathering (*sil*), carbonate weathering (*carb*; including both calcite and dolomite), and gypsum dissolution (*gy**ps*). The contribution of each of these processes to the solute load of the springs can be estimated using a combination of mixing equations, provided that geochemical tracers that are conservative during mixing of compositionally different waters can be identified, and that the composition of the end members can be assessed. Here we use two such tracers:  $^{87}\text{Sr}/^{86}\text{Sr}$  and Na/Sr ratios (all corrected from rain and anthropogenic inputs, as explained in the main text). Indeed, the  $^{87}\text{Sr}/^{86}\text{Sr}$  ratio is not affected by isotope fractionation due to the way data are reduced after measurements by mass spectrometry; and both Na and Sr are soluble elements unlikely to be scavenged into secondary solids such as clays in most contexts. Two mixing equations, each based on one of the two tracers, can be combined with a third summation equation to solve for  $X_{sil}^{Sr}$ ,  $X_{carb}^{Sr}$ , and  $X_{gy\text{ps}}^{Sr}$ , the relative contribution of the three identified end member to dissolved Sr:

$$\left(\frac{^{87}\text{Sr}}{^{86}\text{Sr}}\right)_{spring} = X_{sil}^{Sr} \left(\frac{^{87}\text{Sr}}{^{86}\text{Sr}}\right)_{sil} + X_{carb}^{Sr} \left(\frac{^{87}\text{Sr}}{^{86}\text{Sr}}\right)_{carb} + X_{gy\text{ps}}^{Sr} \left(\frac{^{87}\text{Sr}}{^{86}\text{Sr}}\right)_{gy\text{ps}} \quad (\text{S1})$$

$$190 \quad \left(\frac{\text{Na}}{\text{Sr}}\right)_{spring} = X_{sil}^{Sr} \left(\frac{\text{Na}}{\text{Sr}}\right)_{sil} + X_{carb}^{Sr} \left(\frac{\text{Na}}{\text{Sr}}\right)_{carb} + X_{gy\text{ps}}^{Sr} \left(\frac{\text{Na}}{\text{Sr}}\right)_{gy\text{ps}} = X_{sil}^{Sr} \left(\frac{\text{Na}}{\text{Sr}}\right)_{sil} \quad (\text{S2})$$

$$X_{sil}^{Sr} + X_{carb}^{Sr} + X_{gy\text{ps}}^{Sr} = 1 \quad (\text{S3})$$

The simplification of eq. (S2) is made possible by the fact that the gypsum and carbonate end members can be assumed to be devoid of Na. This assumption is supported by the positions of the different springs in a Na/Sr vs.  $^{87}\text{Sr}/^{86}\text{Sr}$ , which indicates that the low- $^{87}\text{Sr}/^{86}\text{Sr}$  component, encompassing both carbonate and gypsum weathering of the springs has a negligible Na content, with the exception of spring S12 which we do not treat quantitatively here (Fig. S9).



200 Figure S9: Na/Sr vs  $^{87}\text{Sr}/^{86}\text{Sr}$  for the different groups of water outflows (circles represent spring water composition corrected for rain and anthropogenic inputs (eq. 1); triangles represent spring water composition corrected for gypsum dissolution sampled in the S echilienne massif. The inferred composition of the silicate end member for each group is shown as squares

The composition of the end members was constrained as follows (values also provided in Table S1):

- for each spring,  $\left(\frac{^{87}\text{Sr}}{^{86}\text{Sr}}\right)_{spring}$  and  $\left(\frac{\text{Na}}{\text{Sr}}\right)_{spring}$  were taken to be equal to the average ratios (corrected from rain inputs for Na/Sr) over all measurements available for the spring (note that one outlier were dismissed for each of the two springs G1 and G2);
- $\left(\frac{^{87}\text{Sr}}{^{86}\text{Sr}}\right)_{carb}$  was taken between 0.7090 and 0.7095 or 0.7095 and 0.7105, depending on whether the carbonate end member was assumed to be of calcitic or dolomitic nature. These ranges were constrained based on our own geochemical analyses of rock samples (Tab. 1; data available at 10.5281/zenodo.4606732). Note that the first range is consistent with what is known of early Jurassic seawater Sr isotope composition (MacArthur and Howarth, 2004).  $\left(\frac{^{87}\text{Sr}}{^{86}\text{Sr}}\right)_{gyp}$  was taken between 0.7075 and 0.7080, which is typical of Triassic seawater, and in agreement with values reported for Alpine gypsum by previous studies (Kloppmann et al., 2017).
- $\left(\frac{^{87}\text{Sr}}{^{86}\text{Sr}}\right)_{sil}$  was assumed to be equal to the highest measured Sr isotope ratio throughout the local bedrock samples ("micaschist",  $0.735 \pm 0.005$ ; Tab. 1).
- To determine the  $\left(\frac{\text{Na}}{\text{Sr}}\right)_{sil}$  ratio for each of the springs the most affected by silicate weathering (G1, G2, and S10), we extrapolated the Na/Sr vs.  $^{87}\text{Sr}/^{86}\text{Sr}$  relationships passing through (1) the carbonate end member ( $^{87}\text{Sr}/^{86}\text{Sr} = 0.7090-0.7105$  and  $\text{Na}/\text{Sr} = 0$ ) and (2) the samples collected for this spring (Fig. S9) to a  $^{87}\text{Sr}/^{86}\text{Sr}$  equal to that of the silicate end member (0.735, see above). Linear extrapolation in this diagram is made possible by the fact that Sr concentration is present on the denominator of both ratios plotted. Note that following the discussion on Cl sources in section 5.1.1 of the main text, for each of the springs G1, G2, and S10 two estimations of  $\left(\frac{\text{Na}}{\text{Sr}}\right)_{sil}$  were performed: one based on Na concentrations corrected from rain inputs only following eq. (1) ( $[\text{Na}^*]$ ), and the other assuming that the entirety of  $\text{Cl}^-$  release to the springs was associated with  $\text{Na}^+$  release ( $[\text{Na}]-[\text{Cl}]$ ). The average between these two estimates was then used for further calculations. The obtained  $\left(\frac{\text{Na}}{\text{Sr}}\right)_{sil}$  values range from  $80 \pm 9$  to  $205 \pm 30$  mol/mol, lower than those classically estimated for silicates (e.g. Négrel et al., 1993) but consistently with the fact that the parent rock at Séchilienne is a micaschist, that is a sedimentary rock that has lost soluble elements such as Na in previous weathering episodes compared to igneous silicates. For the springs the least affected by silicate weathering (S12, S13, S15, S18, S20, and S21), as such extrapolation would lack precision, we simply took the average and standard deviation of the  $\left(\frac{\text{Na}}{\text{Sr}}\right)_{sil}$  ratios estimated for springs G1, G2, and S10 (yielding  $162 \pm 40$ ). This strong assumption does not bear consequence on our overall evaluation as these former springs are not significantly affected by silicate weathering anyway.

The uncertainty on the different input parameters was propagated to the output variables ( $X_{sil}^{Sr}$ ,  $X_{carb}^{Sr}$ , and  $X_{gyp}^{Sr}$ ) using a Monte Carlo method based on 10,000 iterations. For this, at each of the 10,000 iterations a value for each input parameter (end member composition) was randomly picked following either (a) a normal distribution with mean equal and standard deviations to the estimate and uncertainty provided above, respectively, for parameters  $\left(\frac{^{87}\text{Sr}}{^{86}\text{Sr}}\right)_{sil}$  and  $\left(\frac{\text{Na}}{\text{Sr}}\right)_{sil}$ ; and (b) a uniform distribution bounded by the lowest and highest estimates provided above for parameters  $\left(\frac{^{87}\text{Sr}}{^{86}\text{Sr}}\right)_{carb}$  and  $\left(\frac{^{87}\text{Sr}}{^{86}\text{Sr}}\right)_{gyp}$ .

The choice of a uniform distribution to reflect uncertainty on the latter parameters is justified by the fact that it is highly unlikely that Sr isotope ratios of marine carbonates lie outside of the prescribed range, which is unavoidable to occur for a significant number of random draws if one were to be used a normal distribution with a reasonable standard deviation instead. Note that, generally speaking, the composition of the springs was not considered as a random variable here and was simply fixed for all iterations. However, in order to account for uncertainty on the Cl<sup>-</sup> source to the spring waters (main text section 5.1.1), for each spring and for each simulation we randomly drew values of  $\left(\frac{Na}{Sr}\right)_{spring}$  following a uniform distribution bounded by [Na\*] and [Na]-[Cl]. Finally, Monte Carlo runs yielding  $X_{sil}^{Sr}$ ,  $X_{carb}^{Sr}$ , and  $X_{gyp}^{Sr}$  values outside of the range [0,1] were dismissed (the number of "valid" iterations is reported in Table S2).

The resulting distributions of output  $X_{sil}^i$  values are reported in Table S2 as their 16<sup>th</sup>, 50<sup>th</sup> (median), and 84<sup>th</sup> percentile. Median estimates of  $X_{sil}^{Sr}$  range from 0.06 and 0.08 (springs S15 and S18) to 0.42 and 0.47 (springs G2 and G1, respectively); median estimates of  $X_{carb}^{Sr}$  range from 0.04 and 0.07 (springs S15 and S18) to 0.36 (spring S10); and median estimates of  $X_{gyp}^{Sr}$  range from 0.25 and 0.29 for G1 and G2 to 0.85-0.90 for S18-S15. S10 median estimate is 0.42. Obtained values differed weakly depending on whether a calcitic or a dolomitic composition was used for  $\left(\frac{^{87}Sr}{^{86}Sr}\right)_{carb}$  (Tab. S2).

### Gypsum contribution

The contribution of each of these end members to the load of the dissolved major species SO<sub>4</sub>, Ca, and Mg is necessary to evaluate the impact of the different weathering processes to the CO<sub>2</sub> budget of the S echilienne area (Torres et al., 2016). In principle, these end member contributions to major dissolved species can be calculated from the corresponding contributions to dissolved Sr following:

$$X_i^E = X_i^{Sr} \left(\frac{E}{Sr}\right)_i / \left(\frac{E}{Sr}\right)_{spring} \quad (S4)$$

with  $i = sil, carb, \text{ or } gyp$ , and  $E = SO_4 \text{ and } Mg$  (corrected for rain and anthropogenic inputs). As explained below, because secondary carbonate formation might occur at S echilienne and thus lead to the preferential scavenging of Ca from waters, eq. (S4) cannot be used indifferently for  $E = Ca$  or for  $i = carb$ . We return to the estimation of  $X_i^{Ca}$  values later. Regardless of this issue, eq. (S4) can first be used to calculate  $X_{gyp}^{Mg}$  and  $X_{gyp}^{SO_4}$  provided that the  $\left(\frac{E}{Sr}\right)_{gyp}$  ratios are known. The E/Sr ratios of the gypsum end member were determined using the E/SO<sub>4</sub> vs. (Ca+Mg)/SO<sub>4</sub> relationships described by the springs the least affected by silicate weathering (as identified by their low <sup>87</sup>Sr/<sup>86</sup>Sr ratios, *i.e.* springs S13, S15, S18, S20, and S21; Fig. S10). Indeed, for these springs where sulfate can be assumed to be entirely derived from gypsum and not from sulfide dissolution, at (Ca+Mg)/SO<sub>4</sub> of 1 mol/mol, the entirety of the dissolved load can be assumed to be derived from gypsum dissolution alone (Ca and Mg being the two major cations likely to be released by gypsum dissolution).

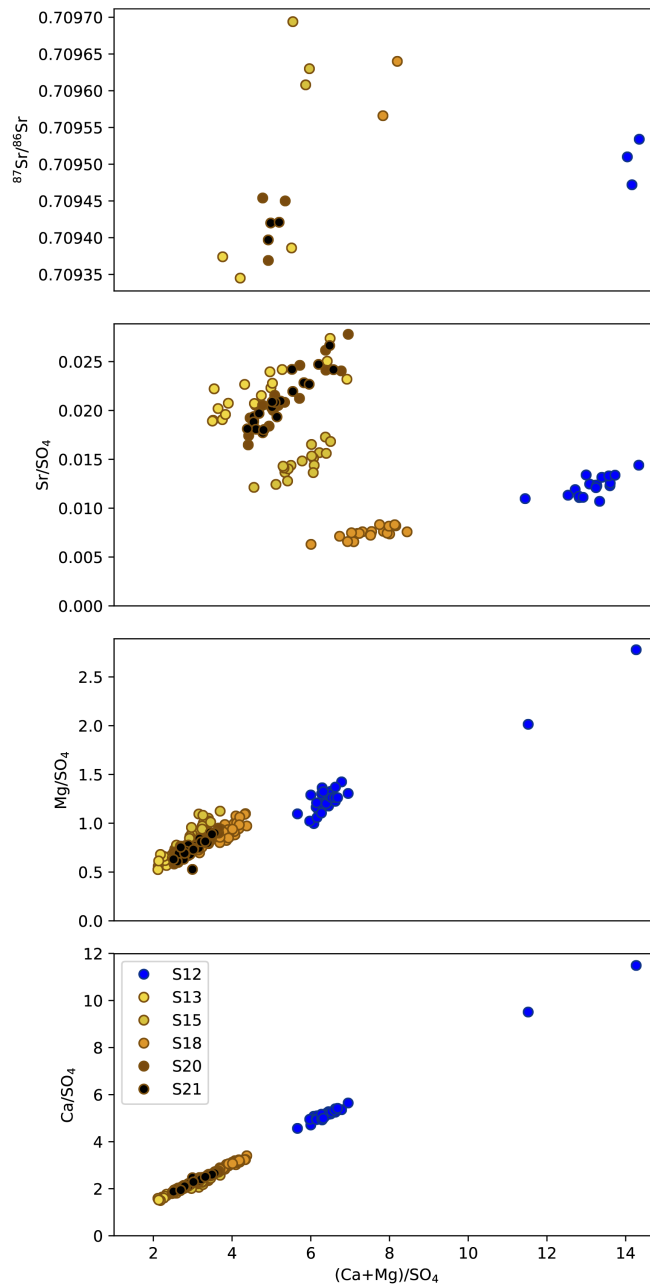


Figure S10: Mixing diagrams of the  $^{87}\text{Sr}/^{86}\text{Sr}$  ratio and the E/SO<sub>4</sub> (with E = Sr, Mg, Ca, and Na) molar ratio vs. the (Ca+Mg)/SO<sub>4</sub> molar ratios, used to determine the E/Sr molar ratios of the gypsum end member.

275 Linear extrapolation in Fig. S10 is made possible by the fact that SO<sub>4</sub> concentration is present on the denominator of both ratios plotted. Taking the average values obtained through extrapolation of the observed trends to (Ca+Mg)/SO<sub>4</sub> = 1 mol/mol suggests  $0.31 \pm 0.04$  and  $9.2 \cdot 10^{-3} \pm 4.4 \cdot 10^{-3}$  mol/mol for the Mg/SO<sub>4</sub> and Sr/SO<sub>4</sub> ratios of the gypsum end members. From these two SO<sub>4</sub>-normalized ratios, Sr-normalized ratios can be obtained to calculate  $X_{gyp}^{Mg}$  and  $X_{gyp}^{SO_4}$  using eq. (S4). Obtained modal values of  $X_{gyp}^{Mg}$  are lower than 0.03 for springs G1-G2-S10, and around 0.20-0.40 for the other springs. Modal values

280 of  $X_{gyp}^{SO_4}$  are lower than 0.05 for springs G1-G2-S10, and range between 0.5 and 0.75 for the other springs.

As the SO<sub>4</sub>/Sr ratio of the carbonate end member was assumed to be equal to 0, consistently with the mixing diagrams of Fig. 4,  $X_{sil}^{SO_4}$  could be calculated as  $1 - X_{gyp}^{SO_4}$  (eq. S3). Consequently, a value for the SO<sub>4</sub>/Sr ratio of the silicate end member could be estimated using the SO<sub>4</sub>/Sr mixing equation (similar to eqs. (S1-S2)):

$$285 \quad \left(\frac{SO_4}{Sr}\right)_{spring} = X_{sil}^{Sr} \left(\frac{SO_4}{Sr}\right)_{sil} + X_{gyp}^{Sr} \left(\frac{SO_4}{Sr}\right)_{gyp} \quad (S5)$$

To solve eq. (S5), the average and standard deviation of all measurements of  $\left(\frac{SO_4}{Sr}\right)_{spring}$  were used, thereby yielding a spring-specific value for  $\left(\frac{SO_4}{Sr}\right)_{sil}$ . This estimate was performed during the Monte Carlo iterations described above, yielding modal values ranging from 666 (spring S20) to 1,845 mol/mol (spring G2).

290

### *Secondary carbonate formation and carbonate contribution*

The precipitation of secondary carbonates is known to preferentially scavenge dissolved  $Ca^{2+}$  at the expense of other alkali-  
 295 earth ions  $Mg^{2+}$  and  $Sr^{2+}$  (Bickle et al., 2015). As a consequence, Ca does not necessarily behave conservatively in carbonate-rich settings such as Séchilienne, where secondary carbonate precipitation is likely to occur. We quantify the role of secondary carbonate formation using the method proposed by Bickle et al. (2015), which is based on the comparison between the chemical composition of springs and that predicted from conservative mixing between the rock dissolution end members. The Rayleigh-type equation proposed by Bickle et al. (2015) links dissolved E/Ca ratios to the extent of Ca  
 300 scavenging by the formation of secondary carbonates:

$$\left(\frac{E}{Ca}\right)_p = \left(\frac{E}{Ca}\right)_0 \gamma^{K_d^E - 1} \quad (S6)$$

where  $\left(\frac{E}{Ca}\right)_0$  is the "initial" E/Ca ratios of waters (*i.e.*, before secondary carbonate precipitation has taken place)  
 305 with E = Sr, Mg, or Na,  $\left(\frac{E}{Ca}\right)_p$  is the E/Ca ratios of waters after secondary carbonate precipitation has taken place,  $\gamma$  is the amount of "initial" Ca left in solution after secondary carbonate precipitation has taken place, and  $K_d^E$  is the partition coefficient of element E into calcite, defined as the ratio between the E/Ca ratio into the precipitating calcite and that in water. During our Monte Carlo simulations, we randomly drew values for  $K_d^{Sr}$  and  $K_d^{Mg}$  following a uniform distribution between 0.02 and 0.10, and considered that  $K_d^{Na} = 0$ . As explained by Bickle et al. (2015), results in terms of source  
 310 apportionment do not depend strongly on the exact values chosen for the  $K_d^E$  parameters.

In a first set of attempts we assumed that secondary carbonate precipitation at Séchilienne was affecting only waters and solutes derived from two of the three rock dissolution end members (*i.e.* silicate and carbonate rocks, silicate rocks and gypsum, or carbonate rocks and gypsum). We assume that secondary carbonate precipitation affects solutes derived from the three weathering sources (carbonate, silicate, and gypsum dissolution) after they are mixed. Such scenario probably does not  
 315 reflect perfectly the reality of the interplay between water mixing and chemical reactions in the subsurface at Séchilienne, but account for the fact that solutes from the three rock dissolution end members are mixed in a complex porous media, while keeping this problem mathematically tractable.

In the compositional Sr/Ca-Mg/Ca-Na/Ca space, the mixing array between carbonate, silicate, and gypsum dissolution is a plane, to which the composition of the springs can be "brought back" (Bickle et al., 2015):

320

$$\alpha \gamma^{1-K_d^{Mg}} \left(\frac{Mg}{Ca}\right)_p + \beta \gamma^{1-K_d^{Sr}} \left(\frac{Sr}{Ca}\right)_p + \epsilon \gamma \left(\frac{Na}{Ca}\right)_p = \delta \quad (S7)$$

where  $\alpha$ ,  $\beta$ ,  $\varepsilon$ , and  $\delta$  are the parameters of the Cartesian equation of the mixing plane in the Sr/Ca-Mg/Ca-Na/Ca space. Note that eq. (S7) is valid because Na is not significantly incorporated into secondary carbonates (in other words,  $K_d^{Na}$  is assumed to be equal to 0). The ternary mixing relationships in the Sr/Ca-Mg/Na-Na/Ca space were constrained for Séchilienne using our own geochemical analyses of rock samples (Tab. 1) and are shown in Fig. S11. These relationships thus allow us to solve numerically eq. (S7) for  $\gamma$  for each spring. We performed this calculation for various values of the relative contribution of dolomite dissolution to the overall Ca released to solution by carbonate weathering (from 0% to 100% dolomite, the rest being delivered by calcite dissolution; the two extreme cases are illustrated in Fig. S11), and constrained the chemical ratios of each of the carbonate components by our own geochemical analyses of rock samples (Tab. 1). We observed as a general trend that increasing the relative contribution of the dolomite end member beyond 20% resulted in an extent of alkalinity consumption through carbonate precipitation that was too large compared to alkalinity production to be sustainable. As a consequence, we fixed the relative contribution of dolomite to the overall Ca release by carbonate dissolution to 10% in the following calculations.

With these constraints, across the Monte Carlo simulations median estimates of  $\gamma$  are 0.38 for G1, 0.39 for G2, 0.40 for S10, and 0.90 for S15. For the other springs,  $\gamma$  was set to 1.00 as no Ca scavenging was required to explain the data - in other words, for these springs the hydrochemical data approximately lie on the mixing plane between the three rock dissolution end members in the Sr/Ca-Mg/Ca-Na/Ca compositional space.

The  $\gamma$  value found for each spring can then be used to provide a value for the dissolved Sr/Ca, Mg/Ca, and Na/Ca ratios before the carbonate precipitation has taken place  $\left(\frac{E}{Ca}\right)_0$  using eq. (S6) with the measured spring ratios as values for  $\left(\frac{E}{Ca}\right)_p$ . Then,  $X_{carb}^{Ca}$  and  $X_{carb}^{Mg}$  can be estimated from eq. (S4) for  $i = carb$ , but using the above-inferred Ca/Sr and Mg/Sr ratios (calculated from Sr/Ca and Mg/Ca ratios) before secondary carbonate precipitation as values of  $\left(\frac{E}{Sr}\right)_{spring}$ .  $X_{sil}^{Ca}$  and  $X_{sil}^{Mg}$  are then determined by difference using eq. (S3) with Ca or Mg instead of Na. Finally, knowing the composition of the carbonate end member (as constrained by our geochemical analyses on rock samples; Tab. 1), values for  $\left(\frac{Ca}{Sr}\right)_{sil}$  and  $\left(\frac{Mg}{Sr}\right)_{sil}$  can be determined using eq. (S2) with Ca and Mg instead of Na, respectively.

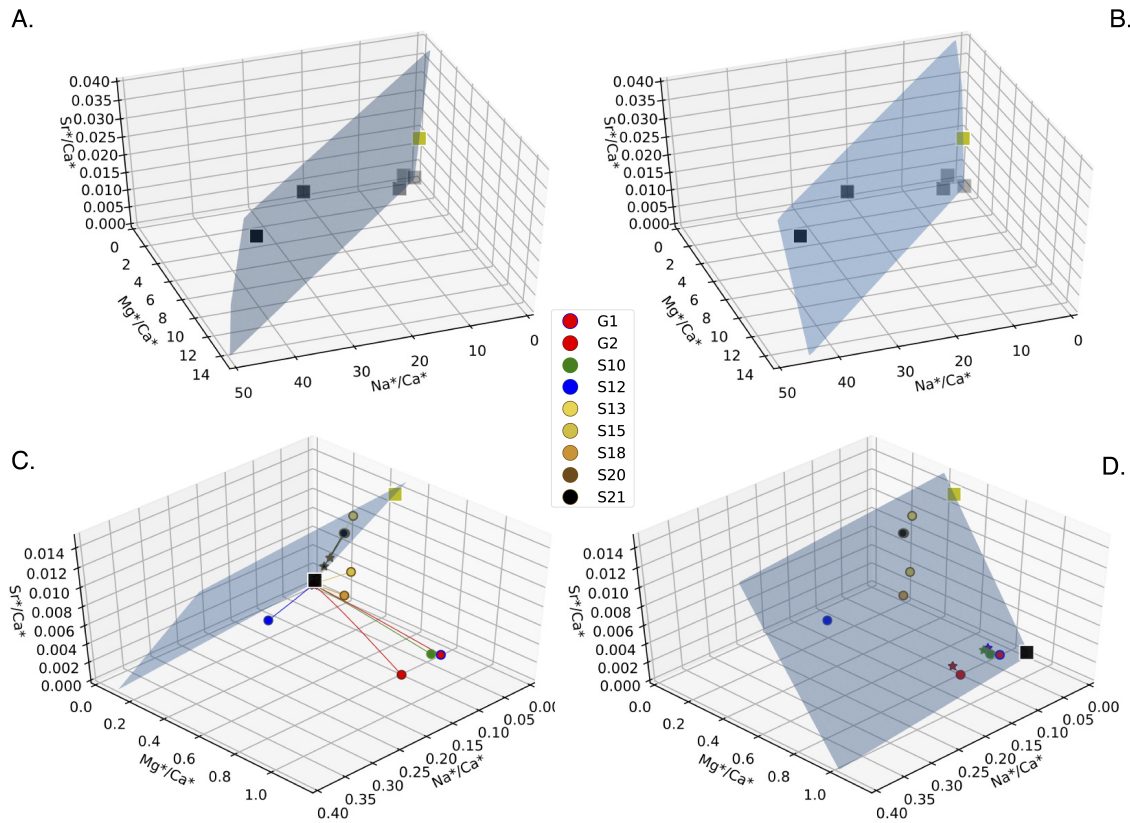
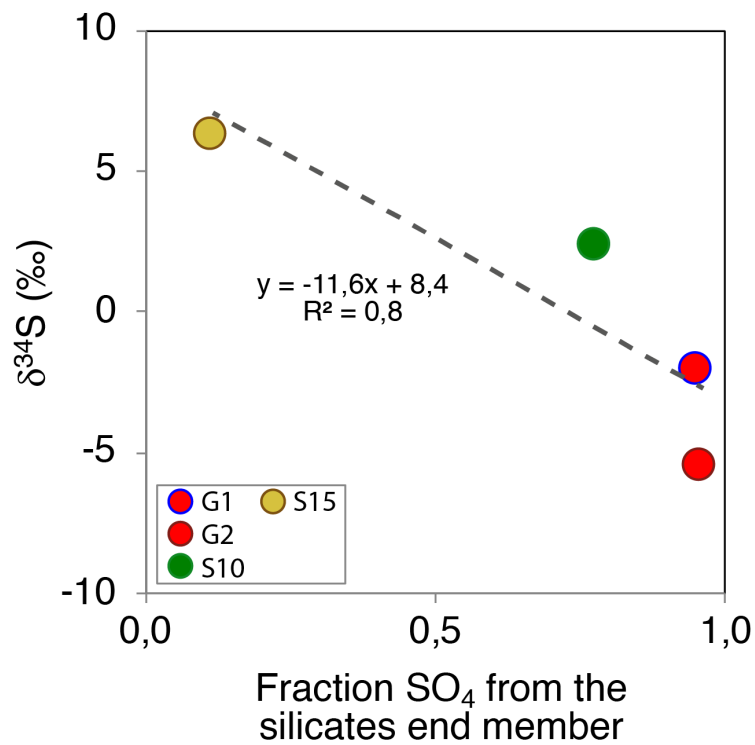


Figure S11: Quantification of the extent of secondary carbonate precipitation on dissolved Ca scavenging. Circles represent spring water composition corrected for rain and anthropogenic inputs (eq. 1) and stars represent spring water composition corrected for secondary carbonate precipitation (hence resulting from conservative mixing only) using the method of Bickle et al. (2015) (eq. S7). The blue plane reflects the ternary mixing between waters derived from carbonate, silicate and evaporite dissolution, as constrained by our geochemical analyses of rocks samples (Tab. 1), on which spring composition must lie after correction from the effect of secondary carbonate precipitation. To obtain these results, all spring Cl<sup>-</sup> was assumed to be associated to Na<sup>+</sup> (main text section 5.1.1), and  $K_d^{Sr}$  was assumed to be equal to  $K_d^{Mg}$  with a value of 0.06 was used.

To assess the validity of our findings from the mixing model using independent measurements, our  $\delta^{34}\text{S}$  measurements can be used. A significant linear negative relationship ( $R^2 = 0.8$ ) exists between the  $\delta^{34}\text{S}$  measured in springs across the S echilienne massif and the modal estimates of their  $X_{sil}^{SO_4}$ , consistent with the isotope composition of sulfur being driven by a binary mixture (Tab. S3; Fig. S12). The intercept of this relationship ( $X_{sil}^{SO_4} = 0$ , equivalent to  $X_{gyp}^{SO_4} = 1$ ) yields an estimate for  $\delta^{34}\text{S}_{gyp} = 8.4\%$ , while extrapolation to  $X_{sil}^{SO_4} = 1$  indicates  $\delta^{34}\text{S}_{sulfur} = -3.1\%$ . Such estimates are fully consistent with our own measurements of solid sulfur at S echilienne, as well as with reported measurements for Triassic seawater where local gypsum might have formed.



365 Figure S12:  $\delta^{34}\text{S}$  measured in springs across the S echilienne massif vs modal estimates of their fraction of  $\text{SO}_4$  from silicate endmember:  
 $X_{sil}^{\text{SO}_4}$ .

370

*CO<sub>2</sub> consumption budget*

The mixing analysis presented above shows that at S echilienne solutes are released to springs through the partial dissolution of silicate minerals, carbonate minerals, and gypsum, while dissolved Ca is scavenged by secondary carbonate precipitation. Fundamentally, these weathering reactions modify the carbon content in the atmosphere-hydrosphere continuum, which impacts the CO<sub>2</sub> concentration in the atmosphere. An approach to evaluate this impact has been recently proposed by Torres et al. (2016), based on the relative change in alkalinity (Alk) and Dissolved Inorganic Carbon (DIC) in ambient waters resulting from the combination of weathering reactions. Torres et al. (2016) contend that the relevant Alk/DIC ratio against which the shifts in Alk and DIC ensuing weathering reactions have to be evaluated is that of the ocean.

375  
 380 However, the approach proposed by Torres et al. (2016) cannot be used in the case of S echilienne, in particular because secondary carbonate precipitation is a significant process there. Indeed, secondary carbonate precipitation removes Alk and DIC from ambient waters following the reaction:



385

And the ensuing change in Alk and DIC occurs at the loci of secondary carbonate precipitation (i.e. at S echilienne, in the subsurface of the instability), the Alk/DIC of which is not known. However, we still believe that it is essential to assess the long-term (that is, once weathering-derived solutes are delivered to the oceans) effects of these weathering reactions on atmospheric CO<sub>2</sub>, especially in contexts where sulfide oxidation is a significant process, such as at S echilienne.

390 As a consequence, we assess the CO<sub>2</sub> impact of the various weathering reactions at S echilienne in the following way (Tab. S3):

- 395
- For silicate weathering by carbonic acid (eq. 9 of main text), each meq of cation released leads to the consumption of 1 mole of CO<sub>2</sub> "on site", meaning immediately when the reaction takes place; and we assume that all meq of cation released are precipitated in the ocean on the "long term" through equation (S9), leading in total to the net consumption of 0.5 mole of CO<sub>2</sub> per meq initially released;
  - Silicate weathering by sulfuric acid (eq. 10), has no "on site" net effect on atmospheric CO<sub>2</sub>; and we assume that it has no net effect on the "long term" either once solutes are delivered to the ocean, based on the fact that this reaction does not produce any alkalinity that is required for carbonate precipitation to occur (eq. S9);
  - 400 • Carbonate weathering by carbonic acid (eq. 11 of main text) consumes 0.5 mol of CO<sub>2</sub> per meq of cation (Ca<sup>2+</sup> or Mg<sup>2+</sup>) released "on site", but this effect is negated on the "long term" by carbonate precipitation in the ocean (eq. S9; note that here "long term" refers to a time scale longer than the characteristic time scale for carbonate precipitation in the ocean (around 10<sup>5</sup> yrs), but shorter than the characteristic time scale for sulfate reduction in the ocean (around 10<sup>7</sup> yrs; Torres et al., 2016));
  - 405 • Carbonate weathering by sulfuric acid (eq. 12 of main text) has no "on site" net effect on atmospheric CO<sub>2</sub>; but is likely to lead on the long term to the release of 0.25 mol of CO<sub>2</sub> (eq. S9) for each meq of cation (Ca<sup>2+</sup> or Mg<sup>2+</sup>) released initially.
  - Secondary carbonate formation happens only "on site" by definition, and leads to the release of 0.5 mol of CO<sub>2</sub> for each meq of cation (Ca<sup>2+</sup>) precipitated (eq. S9).

Given that we do not have access to water discharge at Séchilienne, this analysis cannot be performed on a flux basis. 410 Therefore, we use a concentration-based analysis, where the CO<sub>2</sub> effect of each process is compared within each spring in a consistent manner and expressed as the consumption or release of CO<sub>2</sub> in mol per liter of water (Fig. 7).

We performed this analysis on all springs but spring S12, for which the significant influence of anthropogenic activities precludes quantitative apportionment by the methods outlined above. In addition, in the cases of springs S20 and S21 none 415 of the 10,000 Monte Carlo runs were able to yield  $X_i^E$  values in the interval [0,1] for all  $i$  and  $E$ . This is probably because their hydrochemistry can be readily explained by a simple binary mixture between gypsum and carbonate-derived solutes, such that any small variation in the composition of these end members result in negative  $X_{sil}^E$  values for one or more instances of the element  $E$ . However, because the hydrochemistry of springs S20 and S21 is similar to those of S13 and S15, we expect that their role on atmospheric CO<sub>2</sub> is similar to that played by springs S13 and S15 (Fig. 7).

420

425

430

435 **References**

Bickle, M. J., Tipper, E. T., Galy, A., Chapman, H., and Harris, N.: On Discrimination Between Carbonate and Silicate Inputs to Himalayan Rivers, *Am. J. Sci.*, 315, 120–166, <https://doi.org/10.2475/02.2015.02>, 2015

440 Kloppmann, W., Leroux, L., Bromblet, P., Pogam, P.-Y., Cooper, A., Worley, N., Guerrot, C., Montech, A., Gallas, A., Aillaud, R.: Competing English, Spanish, and French alabaster trade in Europe over five centuries as evidenced by isotope fingerprinting. *Proceedings of the National Academy of Sciences*. 114. 201707450. [10.1073/pnas.1707450114](https://doi.org/10.1073/pnas.1707450114), 2017

McArthur, J. and Howarth, R.: *Strontium Isotope Stratigraphy*. [10.1016/B978-0-444-59425-9.00007-X](https://doi.org/10.1016/B978-0-444-59425-9.00007-X), 2004

445

Négrel, P., Allègre, C. J., Dupré, B., Lewin, E.: Erosion sources determined by inversion of major and trace element ratios and strontium isotopic ratios in river: The Congo Basin case, *Earth and Planetary Science Letters*, 120(1–2), 59–76, [https://doi.org/10.1016/0012-821X\(93\)90023-3](https://doi.org/10.1016/0012-821X(93)90023-3), 1993

450 Torres, M. A., West, A. J., Clark, K. E., Paris, G., Bouchez, J., Ponton, C., Adkins, J. F.: The acid and alkalinity budgets of weathering in the Andes–Amazon system: Insights into the erosional control of global biogeochemical cycles. *Earth and Planetary Science Letters*, 450, 381–391, <https://doi.org/10.1016/j.epsl.2016.06.012>, 2016

455